Journal of Non-Crystalline Solids 594 (2022) 121826

Contents lists available at ScienceDirect

Journal of Non-Crystalline Solids

journal homepage: www.elsevier.com/locate/jnoncrysol

Tailoring multiphonon relaxation and cross relaxation energy transfer in mixed ionic-electronic $20Li_2O$-xBi_2O_3-$(78-x)TeO_2$-$1Er_2O_3$-1Ag glasses at NIR region

M.S. Sutrisno [a,c], H. Nurhafizah [b], N.S. Sabri [d], R. Hisam [a,*]

[a] Faculty of Applied Sciences, Universiti Teknologi MARA, Shah Alam, Selangor 40450, Malaysia
[b] Advanced Optical Materials Research Group, Faculty of Science, Universiti Teknologi Malaysia, Skudai, Johor 81310, Malaysia
[c] University of Cyberjaya (UoC), Persiaran Bestari, Cyber 11, Cyberjaya, Selangor 63000, Malaysia
[d] Faculty of Applied Sciences, Universiti Teknologi MARA Pahang, Bandar Tun Abdul Razak, Pahang 26400, Malaysia

ARTICLE INFO

Keywords:
Multiphonon relaxation
Mixed ionic-electronic
Energy transfer

ABSTRACT

A glass composed of $20Li_2O$-xBi_2O_3-$(78-x)TeO_2$-$1Er_2O_3$-1Ag was fabricated by melt–quenching method to examine the influence of mixed ionic–electronic (MIE) effect on AC conductivity (σ_{AC}) and photoluminescence properties. The σ_{AC} decreased as the Bi_2O_3 content increased, until a minimum σ_{AC} at x=11 mol% attributable to the MIE effect was achieved. The photoluminescence intensity and lifetime (τ_{mes}) of the $^4I_{13/2}\rightarrow{}^4I_{15/2}$ transition were reported with a drop at x=11 mol%, coincided with the minimum σ_{AC}. Results on the analysis of the multiphonon relaxation rate (W_{MPR}) revealed that adding low-phonon Bi_2O_3 concentration promoted higher photoluminescence intensity and longer τ_{mes} due to the reduction in W_{MPR}. However, the drop in photoluminescence intensity and τ_{mes} at x=11 mol% may be due to a blocking effect. The blocking effect may have induced nonradiative phonon-assisted S_{ab} and cross-relaxation γ_6 energy transfer, leading to a maximum W_{MPR} and energy transfer parameter.

1. Introduction

Oxide glasses have received a lot of attention due to their unique properties and potential applications in a variety of industries, especially in the fields of optics, photonics, and lasers. Tellurium oxide-based glasses, which have a high glass forming capability [1,2] and a low freezing point [3–5], have intrigued technical interest among oxide glasses. Apart from its high transparency, TeO_2 based glasses are non-hygroscopic, unlike P_2O_5 and B_2O_3 glasses [6]. These tellurite glasses have a high dielectric constant [7], high index of refraction [8,9], and major third-order nonlinear optical susceptibility [10,11] making them a potential optical device material. In addition, low maximum phonon energy glasses such as Bi_2O_3 and TeO_2 doped with rare earth ions (RE) ions had been received a lot of attention due to its potential for optical and laser technologies due to their capability in reducing non-radiative emission [12,13]. A TeO_4 trigonal bipyramid (tbp) and TeO_3 trigonal pyramid (tp) unit structure with a lone pair at the equatorial position characterize the TeO_2 glass fundamental structure [14]. Hence, TeO_2 is an interesting conditional glass former that may change in structure from TeO_4 unit to TeO_3 unit with the addition of a modifier oxide, such as alkali metal oxides and transition metal oxides. Interestingly, the changes of glass former structure may induce changes in maximum lower phonon of the glasses that lead to changes in photoluminescence intensity and lifetime of rare earth doped glasses.

Er^{3+} is the most effective of the RE ions, emitting blue, green, and red emission bands in the visible field, as well as green upconversion luminescence when excited at 980 nm. Then, the fabrication of photonic devices for 1.55 μm amplifications, frequency upconverting blue green lasers, planar waveguides, and temperature sensors has proved to be an excellent application for Er^{3+} doped glasses [15–17]. For green laser applications, the Er^{3+} with $^2H_{11/2}$ (550 nm) emission transition has been extensively studied via upconversion emission [18,19]. On the other hand, recent research has also focused on the NIR spectral emission band originating from the $^4I^4_{9/2}\rightarrow I1_{5/2}$, $^4I_{11/2}\rightarrow{}^4I_{15/2}$, and $^4I_{13/2}\rightarrow{}^4I_{15/2}$ transitions between 800 and 1550 nm due to their emission properties that have broader fluorescence bandwidth and large stimulated emission cross-section [20–22]. The Er^{3+} ion concentration, ion-ion interaction, absorption and emission cross sections, radiative and

* Corresponding author.
E-mail address: rosdiyana@uitm.edu.my (R. Hisam).

https://doi.org/10.1016/j.jnoncrysol.2022.121826
Received 29 March 2022; Received in revised form 13 June 2022; Accepted 16 July 2022
Available online 30 July 2022

non-radiative lifetimes are all relevant parameters to investigate in order to improve Er^{3+} doped optical amplifiers [23]. Generally, higher Er^{3+} ion concentration leads to higher gain, but cluster forming in the form of an Er^{3+}–Er^{3+} ion pair may occur, causing luminescence quenching and energy dissipation, which affects the optical gain of Er^{3+} doped glasses [24]. The basic characterization peak values of the absorption and emission cross-section spectra that can be improved by changing the local electric field around the Er^{3+} ion site may contribute to advancement in EDFA applications. Zavadil et.al recently investigated the composition-dependent spectroscopic properties and Stark level splitting of Er^{3+} ions in the zinc–sodium–antimonite glasses [23]. Furthermore, Kesavulu et al. investigated the structural, thermal, and optical properties of Er^{3+} ions in SiO_2–Al_2O_3– LiF–SrF_2 oxyfluoride glasses and found that the higher Er^{3+} ion concentration will result to higher gain and broad emission at 1.5 μm [13]. Hence, it is interesting to study the effect heavy metal oxides addition such as Bi_2O_3 to Er^{3+} doped glasses to emission and lifetime properties stated above.

As heavy metal oxides (HMO) such as PbO, Bi_2O_3, and V_2O_5 are incorporated into the glass network, they act as both network formers and modifiers, depending on their concentration, and have a lower melting temperature, higher stability, and stable optical properties, as well had low phonon energy. Tellurite glasses have phonon energies in the order of 750 cm^{-1}, whereas other heavy metal oxide containing glasses, such as PbO and Bi_2O_3 have phonon energies around 750–850 cm^{-1} which contribute to the enhancement of luminescence properties of Er^{3+} doped glasses. Furthermore, the addition of heavy metals such as Bi_2O_3 to the tellurite network causes structural changes due to the conversion of TeO_4 to TeO_3 units is closely related to mixed ionic-electronic effect. Mixed ionic-electronic glass is a glass with mixed ionic and electronic conductivity properties, can be made by combining glass networks (i.e. TeO_2) with alkali metal oxides (i.e. Li_2O), and transition metal oxides such as (i.e. Bi_2O_3) [25]. Ionic conductivity in mixed ionic-electronic glass is provided by alkali ions from alkali metal oxide, while electronic conductivity is provided by transition metal ions from transition metal oxide. Previous research on several mixed ionic electronic glasses such as $30Li_2O$-$20ZnO$-xBi_2O_3-$(50-x)SiO_2$ [26] and $10ZnO$–xBi_2O_3–$(90-x)B_2O_3$ [27] reported the anomalous trends on conductivity and dielectric parameters with increasing transition metal oxide. As a result, it was proposed that mixed ionic-electronic glasses are caused by interaction between ionic and electronic carriers in the glass network, either by blocking effect or ion-polaron binding, which contributes to anomalous pattern on conductivity and dielectric properties which named as mixed ionic-electronic effect. Hence, it had been interesting to study the effect of mixed ionic-electronic effect on photoluminescence properties of rare earth doped glasses.

Radiative transfer to another ion and non-radiative transfers, such as multiphonon relaxation, cross relaxation, and energy transfer to impurities, are processes that compete with luminescence. In these cases, energy is lost to the local vibrations of surrounding atoms (phonons) and to electronic states of atoms in the vicinity. As a result, multiphonon relaxations become the primary major obstacle to high quantum efficiency [22,23]. Previous research showed the effect of Bi_2O_3 addition on enhancement of luminescence intensity properties in glasses doped with rare-earth ions due to its low phonon energy such as in $(99.5-x)$ $[(4ZnO-3B_2O_3)]$-$0.5Nd_2O_3$-xBi_2O_3 [28], $20CdO$-xBi_2O_3-$(79.5-x)$ B_2O_3-0.5 Sm_2O_3 [29], and $20ZnO$-$xBi_2O_3(79-x)B_2O_3$-$1Sm_2O_3$ [30] glasses. A strong increase was observed in luminescence quantum yield attributed to the reduction in phonon energy of the host glass which then reduces the non-radiative multiphonon relaxation rates of excited states thereby enhance emission intensity as on $^4F_{3/2}\rightarrow{}^4I_{9/2}$ transition in $[(99.5-x)$ $\{4ZnO-3B_2O_3\}$-$0.5Nd_2O_3$-xBi_2O_3 [28]. Interestingly, luminescence study had been done in $75TeO_2$-$(25-x)ZnO$-xBi_2O_3-$0.5Er_2O_3$ [31] that showed lower probability for a nonradiative transition rate with the addition of Bi_2O_3. Substitution of Bi_2O_3 in glass induces reduction on phonon energy of glass host due to lower phonon energy of Bi_2O_3 compared to TeO_2 which then decrease the probability for nonradiative transition rate. However, quenching in emission intensity was observed in Bi_2O_3 glasses such as on $^5I_6\rightarrow{}^5I_8$ transition at 1.20 mm in Ho^{3+} /Yb^{3+}-co-doped $57PbO$–$25Bi_2O_3$–$18Ga_2O_3$ glasses due to rapid multiphonon deexcitation attributed from small energy gap from $^5I_6$ level to the next lower level $^5I_7$ [32]. Hence, those contrasting emission behaviour between glass samples above showed that the effect of lower phonon Bi_2O_3 to emission behaviour of rare earth doped glasses may still not properly understood.

The fluorescence features of such samples were examined in this article in terms of emission spectra, quantum efficiency, multiphonon relaxation rates, and phonon energy. In this study, the dominant factor for high nonradiative transition rates and decreased quantum efficiency for glass samples was determined. The present work intends to discuss the role of lower phonon Bi_2O_3 on tailoring the multiphonon relaxation and cross relaxation process which induce changes in photoluminescence properties of mixed ionic-electronic $20Li_2O$-xBi_2O_3-$(78-x)$ TeO_2-$1Er_2O_3$-1Ag glasses.

2. Materials and methods

2.1. Preparation of the glasses

The raw materials for making $20Li_2O$-xBi_2O_3-$(78-x)TeO_2$-$1Er_2O_3$-1Ag are available as chemical powders. The chemicals utilized in this study are analytical grade TeO_2, Bi_2O_3, Li_2CO_3, Er_2O_3, and AgCl. The glass samples are fabricated using the melt-quenching technique and have a nominal composition of $20Li_2O$-xBi_2O_3-$(78-x)TeO_2$-$1Er_2O_3$-1Ag where x= 3,5,7,11, and 13 mol%. A sensitive weighing equipment is used to weigh the raw materials in the proper proportions with each batch of glass has a total weight of 6.0 g. The mixture was then homogenized in an agate mortar for an hour before being loaded in an alumina crucible. The mixture is placed in a porcelain crucible and melted for 1 h at 1173 K in an electrical furnace. The glass samples are next quenched and annealed at 623 K for 2 h 30 min to decrease thermal and mechanical stresses. The furnace is turned off after 2 hours 30 min, and the samples are allowed to cool to room temperature. Finally, the samples are polished in preparation for structural and optical analysis.

2.2. Sample characterization

The impedance properties of glass samples were determined by attaching the Solartron Impedance Analyzer 1255/1287 to a sample holder with a 500 mV potential at room temperature and a frequency range of 10^{-3} to 10^6 Hz. The obtained impedance data was fitted to an equivalent circuit for all glass samples using Zview software and fitted Nyquist plot data was used to calculate dielectric constant ε', tan δ, and AC conductivity σ_{AC} using relations shown below:

$$\varepsilon' = Cd/\varepsilon_0 A \tag{1}$$

$$\varepsilon'' = \varepsilon' \tan\delta \tag{2}$$

$$\sigma_{AC} = \omega\varepsilon_0\varepsilon'' \tag{3}$$

where ε_0 is the permittivity constant of free space of dielectric glass sample media, C is the capacitance, d is the thickness of the glass sample, ω is the frequency of the input current signal and A is the cross-sectional area of the glass sample. The sample then analyzed for Raman spectroscopy using ACRON, Confocal Micro Raman at range 115 cm^{-1} to 1200 cm^{-1}. After that, a Shimadzu UV-VIS spectrophotometer with a double-beam for wavelengths of 200 nm to 2500 nm was used to measure the optical absorption of the glass samples. In addition, the photoluminescence spectra and decay rates spectra of the glass samples were measured using a PTI QuantaMaster™ 60 Fluorescence Spectrophotometer in the wavelength range of 200-1700 nm. The fitting of parameters had been done by using Origin 2019 software and the

precision of measurements and calculations had been evaluated by error analysis as displayed by error bars in figures and uncertainty values in tables.

3. Results and analysis

3.1. AC conductivity and dielectric properties

The σ_{AC} with increasing Bi_2O_3 concentration at 10^2 Hz and room temperature had a nonlinear decrease at $x \leq 11$ mol% before a considerable increase at $x > 11$ mol% (Fig. 1). Meanwhile, as the Bi_2O_3 concentration increased, the dielectric constant ε' had an initial large decrease for $x \leq 5$ mol% and subsequent off-trend increase at $x = 7$ mol% before a large decrease at $x > 7$ mol% at room temperature and 10^2 Hz (Fig. 2). The loss tangent tan δ decreased at $x = 5$ mol% before a slight increase at $x = 7$ mol%, followed by a large decrease at $x = 11$ mol% before increasing again at $x > 11$ mol% (Fig. 3).

3.2. Raman analysis

The Raman spectra of the tetrahedral glass structure, such as the TeO_2 glass in the 10–1200 cm^{-1} range could be separated into four areas: the boson area (10–250 cm^{-1}), low-frequency region (250–700 cm^{-1}), medium-frequency region (700–850 cm^{-1}), and high-frequency region (850–1300 cm^{-1}) [33]. As shown in Fig. 4, the Raman spectra of the examined glasses in the 115–1200 cm^{-1} range included five main bands at 165–167, 368–374, 670–676, 747–754, and 825–827 cm^{-1}. The band at 165–167 cm^{-1} was assigned to the boson peak [34,35]. The absorption band at 368–374 cm^{-1} range could be attributed to the Bi–O–Bi stretching vibrations in the distorted BiO_6 octahedral units [36]. The Raman band at 670–676 cm^{-1} range could be assigned to the axially symmetric Te_{ax}–O–Te_{ax} stretching vibrations in the TeO_4 trigonal bipyramids (tbps) unit (where eq and ax refer to equatorial and axial, respectively) [37,38]. The band at 747–754 cm^{-1} could be assigned to the vibrational modes of Te_{eq}–O–Te_{eq}, which is a TeO_4 unit with the axial bond length of deformed TeO_{3+1} polyhedra or Teeq–O in TeO_3 trigonal pyramids (tps), which is one oxygen larger than Te_{eq}–O–Te_{eq}. These vibrational modes were correlated to the Te=O bond stretching in the O=TeO_2 unit [37,38]. Meanwhile, the 825–827 cm^{-1} band may be assigned to the BiO_3 unit. The boson peak, which is a combination of acoustic phonons and rotational molecular modes, provides additional information on the glass structure. Changes in the chemical composition due to the addition of a glass modifier have a significant impact on the elastic constant. The results showed that the peak position shifted, indicating structural changes in the glass network [48]. The shift of the

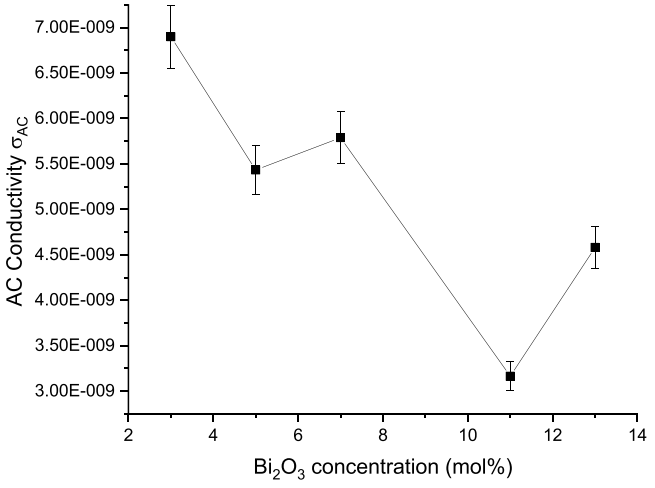

Fig. 1. AC conductivity σ_{AC} pattern of $20Li_2O$-xBi_2O_3-(78-x)TeO_2-$1Er_2O_3$-1Ag glass system with increasing Bi_2O_3 concentration at frequency of 10^2 Hz.

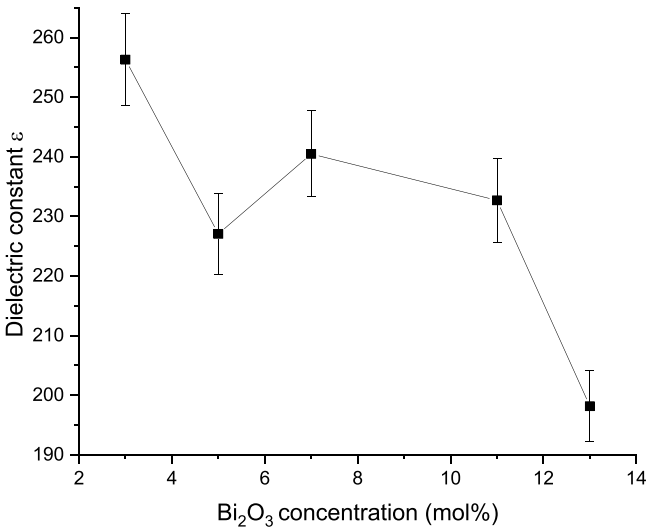

Fig. 2. Dielectric constant ε of $20Li_2O$-xBi_2O_3-(78-x)TeO_2-$1Er_2O_3$-1Ag glass system with increasing Bi_2O_3 concentration at frequency of 10^2 Hz.

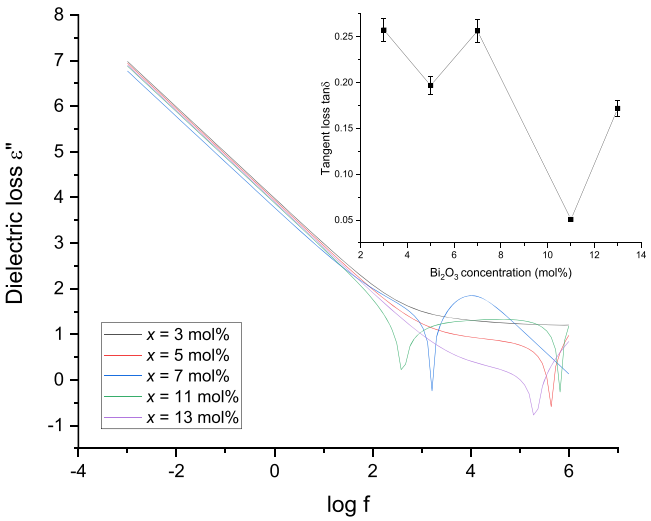

Fig. 3. Dielectric loss ε" of $20Li_2O$-xBi_2O_3-(78-x)TeO_2-$1Er_2O_3$-1Ag glass system with increasing frequency. Inset shows loss tangent tan δ of $20Li_2O$-xBi_2O_3-(78-x)TeO_2-$1Er_2O_3$-1Ag glass system with increasing Bi_2O_3 concentration at frequency of 10^2 Hz.

boson peak to higher Raman shift from $x = 3$ mol% (165.60 cm^{-1}) to $x = 5$ mol% (167.47 cm^{-1}) indicated the opening of the glass network by the glass modifier [39,40]. In addition, the TeO_4 band shifted to higher Raman shift from $x = 3$ mol% (670.65 cm^{-1}) to $x = 5$ mol% (675.92 cm^{-1}), indicating the depolymerization from the TeO_4 unit to the TeO_{3+1}/ TeO_3 unit. This phenomenon contributed to the formation of the nonbridging oxygen (NBO) unit. However, the TeO_4 band shifted to lower wavenumber at $x = 11$ mol% (674.16 cm^{-1}), implying the decrease in the formation of NBOs [37,38]. The increase in relative intensity of the BiO_6 and TeO_3 band peaks from $x = 3$ mol% to $x = 7$ mol% also signified the role of Bi_2O_3 in the formation of the NBO TeO_3 unit before the relative intensity drop at $x = 11$ mol%. This result showed the reduced role of Bi_2O_3 in formation of TeO_3 unit [38]. The deconvolution of the Raman spectrum for $x = 3$ mol% is shown in Fig. 5, and its characteristics are listed in Table 1.

Smaller nonradiative rates and better radiative efficiencies or emission intensities are affected by the lower maximum phonon energy of the glass matrix. The phonon energies related to the last peak in the Raman

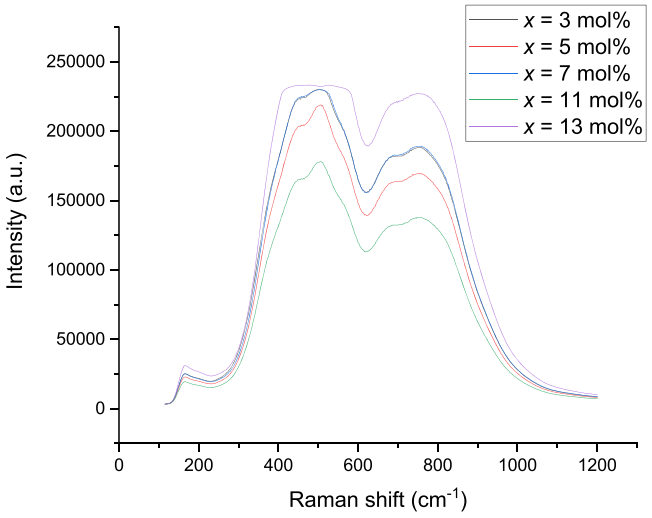

Fig. 4. Raman spectra from 100 to 1200 cm^{-1} of $20Li_2O$-xBi_2O_3-(78-x)TeO_2-$1Er_2O_3$-1Ag glass system with different Bi_2O_3 concentration.

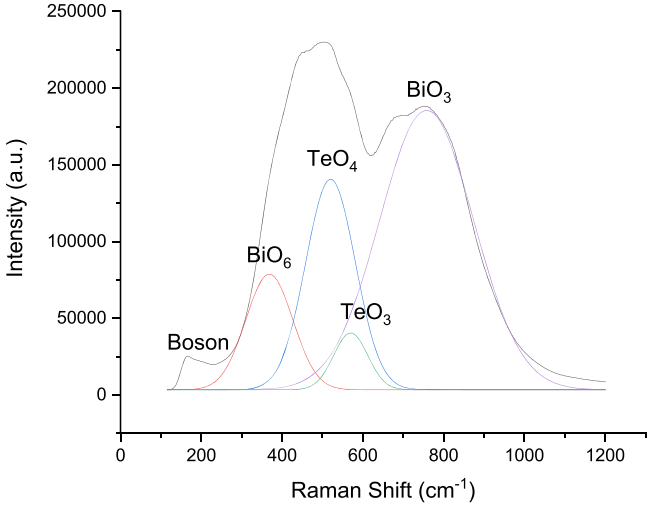

Fig. 5. Raman spectra deconvolution of $20Li_2O$-$3Bi_2O_3$-$75TeO_2$-$1Er_2O_3$-1Ag glass system

spectra showed a slight shift across the different modified samples (Fig. 4) that would affect the emission intensity. Hence, multiphonon relaxation (MPR), which is mainly influenced by the maximum phonon energy of the glass, is considered to have a major effect on emission intensity. In the weak-coupling scenario of RE luminescent centers, the MPR rate W_{MPR} follows an exponential gap rule as follows:

$$W_{MPR} = C\left[\frac{exp(\hbar w_p/KT)}{exp\left(\frac{\hbar w_p}{KT}\right)-1}\right]^p e^{-\alpha\Delta E}, \quad (4)$$

where $P = \frac{\Delta E}{\hbar w_p}$ is the phonon order, ΔE is the energy gap, $\hbar w_p$ is the maximum phonon energy of the host glass, K is Boltzmann's constant, $\alpha = \frac{-\ln(\varepsilon)}{\hbar w_p}$, and C is dependent on the host. From Eq. (4), the multiphonon decay of the RE ions in the glass is generally dependent on the maximum phonon energy of the host glass. Nevertheless, the constant C may also be a key element in determining W_{MPR} based on the Debye approximations, in which

$$C \propto \rho\omega^{5/3}, \quad (5)$$

where $\rho(\omega)$ is the phonon density of state of the glass matrix. As a result of the decreased phonon density, C will be smaller, indicating a weaker MPR and more intense luminescence. The maximum phonon energy, $\hbar w_p$ from the Raman peaks showed an initial shift to higher wavenumber at x=5 mol% (827.03 cm^{-1}) before it shifted to a lower wavenumber at x=7 mol% and x=11 mol% (825.31 cm^{-1}) and then shifted to a higher wavenumber at x=13 mol% (827.03 cm^{-1}). Fig. 4 shows that the intensity of the Raman peaks for these tellurite glasses decrease at x=5 mol %, suggesting the role of Bi_2O_3 in reducing the phonon density $\rho(\omega)$ of the glass that led to the weaker MPR. The phonon density $\rho(\omega)$ may induce changes in the MPR rate, leading to changes in the Er^{3+} emission intensity [41–43]. Meanwhile, the overall increase in the width peak (FWHM) (Table 1) with increasing Bi_2O_3 may indicate the increase in the disorderliness of the glass network probably due to depolymerization caused by Bi_2O_3 [44].

3.3. Decay rates and multiphonon relaxation parameter

The experimental decays of the Er^{3+}: $^4I_{13/2}$ level in the prepared samples at room temperature are shown in Fig. 6. The PL decay curves did not follow a single exponential decay pattern, indicating that the energy transfer mechanism from Er^{3+} ions to Er^{3+} ions and silver NPs to Er^{3+} ions was effective [45]. Deviations from a single exponential decay curve could indicate the presence of nonradiative excitation transfer from rare-earth (RE) interactions [46]. The long lifetime of materials is an essential consideration for a good Er^{3+}-doped fiber laser. In general, the increase in measured fluorescence lifetime is due to an improved local electric field from energy transfer from silver NPs to Er^{3+}, energy transfer from Er^{3+} ions to Er^{3+} ions, and a decrease in the phonon density $\rho(\omega)$ of glass [41,45]. The measured lifetime can be calculated as follows:

$$\tau_{mes} = \frac{1}{I_0}\int I(t)dt, \quad (6)$$

Table 1
Raman Spectra assignments and Centre peak, C_p Integrated area, A_p FWHM and maximum intensity, I_p with respects to their wavenumbers for $20Li_2O$-xBi_2O_3-(78-x)TeO_2-$1Er_2O_3$-1Ag glass samples

x=3 mol%		x=5 mol%		x=7 mol%		x=11 mol%		x=13 mol%		Assignments
FWHM (cm^{-1})	I_p (a.u.)	FWHM (cm^{-1})	I_p (a.u.)	FWHM(cm^{-1})	I_p (a.u.)	FWHM (cm^{-1})	I_p (%)	FWHM(cm^{-1})	I_p (%)	
327.96	138930	331.31	127844	332.23	141121	328.66	100230	335.04	170497	(BiO_6)
621.36	175313	675.91	158467	621.36	177095	616.06	127335	624.89	213879	[TeO_4]
111.52	184930	113.17	166331	88.93	185969	48.68	134719	104.52	223770	[TeO_3]
54.86	157416	66.80	140449	58.28	158940	77.62	115541	78.38	195547	[BiO_3]
x=3 mol%		x=5 mol%		x=7 mol%		x=11 mol%		x=13 mol%		Assignments
C_p (cm^{-1})	A_p (%)	C_p (cm^{-1})	A_p (%)	C_p (cm^{-1})	A_p (%)	C_p (cm^{-1})	A_p (%)	C_p (cm^{-1})	A_p (%)	
368.466	6.6628	372.109	6.8130	372.109	6.6784	368.466	6.4596	373.929	6.8291	[BiO_6]
670.654	7.2907	675.916	8.0495	675.916	8.1181	674.163	8.45859	675.916	7.8698	[TeO_4]
749.231	18.6008	754.441	18.8291	759.649	14.9930	747.493	8.3372	747.493	18.1724	[TeO_3]
825.31	6.5613	827.03	7.4083	825.31	6.9267	825.31	9.8265	827.03	9.7116	[BiO_3]

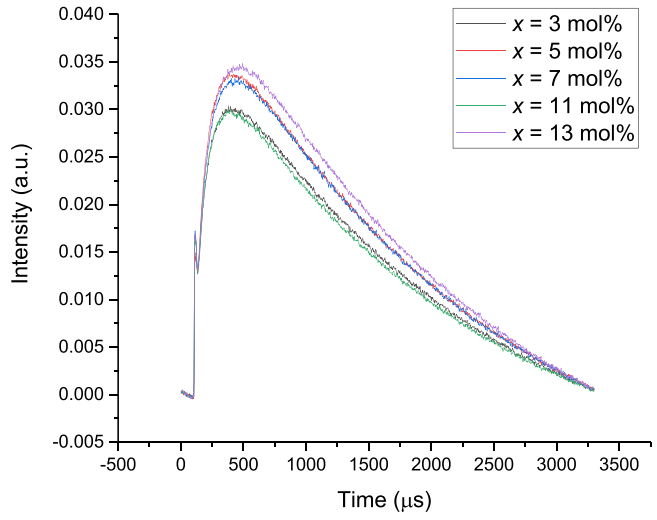

Fig. 6. Room temperature PL decay curves of $^4I_{13/2} \rightarrow {}^4I_{15/2}$ transition, under excitation wavelength λ=980 nm of $20Li_2O$-xBi_2O_3-$(78\text{-}x)TeO_2$-$1Er_2O_3$-1Ag glass system increasing Bi_2O_3 concentration.

where $I(t)$ and I_0 are the PL intensities at time t and at t=0, respectively. The τ_{mes} can be determined by fitting Eq. (6) to decay rates data for all glass samples in Fig. 6. The measured lifetime τ_{mes} (Fig. 7) showed an initial increase before it dropped at x=11 mol% followed by a large increase at x>11 mol%.

Information regarding the rates of various nonradiative processes is required for accurate laser design calculations for a lasing medium. Ion–ion energy transfer, concentration quenching, nonexponential decay, and relaxation by multiphonon emission can affect the quantum efficiency of the laser emission. Multiphonon emission is the primary nonradiative decay mechanism for low concentrations of rare-earth dopant ions [47]. The MPR rate in an excited state is determined by the level energy separation from the next lower lying level that was influenced by the host material, which may be analyzed by its maximum phonon energy $\hbar w_p$ and phonon density $\rho(\omega)$ as reported in the Raman analysis above based on Eq. (4). However, the MPR rate W_{MPR} may also be calculated as follows [47]:

$$W_{MPR} = \frac{1}{\tau_{mes}} - A_{rad}, \tag{7}$$

where τ_{mes} is the measured lifetime, and A_{rad} is the spontaneous emission probability from the Judd-Ofelt calculation. In general, a low maximum phonon energy $\hbar w_p$ and phonon density $\rho(\omega)$ may result in a low nonradiative rate, which enhances the quantum efficiency or emission intensity [41]. The large decrease in the MPR rate W_{MPR} (Fig. 8) at $x \leq 7$ mol% was followed by an increase at $x \geq 11$ mol% with the addition of Bi_2O_3. A high fluorescence efficiency of rare-earth ions, which was evaluated by the value of their quantum efficiency η, i.e., the distribution of lifetime between the radiative and nonradiative transitions, is another crucial criterion for a viable host material. The quantum efficiency η was computed using the radiative lifetime τ_{rad} from the Judd-Ofelt theory and the measured experimental lifetime τ_{mes} as follows[45]:

$$\eta\ (\%) = \frac{\tau_{mes}}{\tau_{rad}}. \tag{8}$$

The quantum efficiency η (Fig. 8) initially increased until it reached a maximum at x=7 mol% and then dropped at $x \geq$ 11 mol%. The maximum η at x=7 mol% indicated a large stimulated emission cross-section (ECS), making it a good option for 1.532 μm amplification. The measured lifetime τ_{mes}, MPR rate W_{MPR}, and quantum efficiency η are listed in Table 2.

The maximum phonon energy $\hbar w_p$ (Fig. 9) initially increased before a large minimum at x=11 mol%, after which it increased sharply at x>11 mol%. Although the MPR rate W_{MPR} was dependent on the maximum phonon energy $\hbar w_p$ of the glass, the logarithm of the MPR rate W_{MPR} also depended on the energy gap ΔE. In general, the phonon number P should be larger than two to bridge the energy gap ΔE [49]. The required phonon number P to bridge the energy gap ΔE of $^4I_{13/2} \rightarrow {}^4I_{15/2}$ of Er^{3+} ions in the glass samples was calculated to be between 7.52 and 7.97 (Table 2), implying that the samples could have a low quantum efficiency [50]. Furthermore, phonon number P (Fig. 9) was initially decreased before a maximum at x=11 mol%, after which it decreased at x>11 mol%. This phenomenon indicates that the largest phonon number required to bridge the energy gap ΔE was at x=11 mol%. Table 2 shows the energy gap ΔE, maximum phonon energy $\hbar w_p$ and phonon number P of $^4I_{13/2} \rightarrow {}^4I_{15/2}$ transition, under excitation wavelength λ=980 nm with increasing Bi_2O_3 concentration.

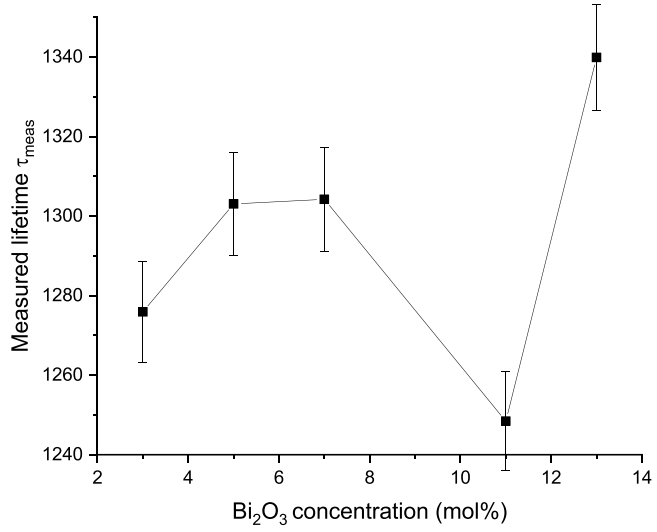

Fig. 7. Measured lifetime τ_{mes} of $^4I_{13/2} \rightarrow {}^4I_{15/2}$ transition, under excitation wavelength λ=980 nm of $20Li_2O$-xBi_2O_3-$(78\text{-}x)TeO_2$-$1Er_2O_3$-1Ag glass system increasing Bi_2O_3 concentration.

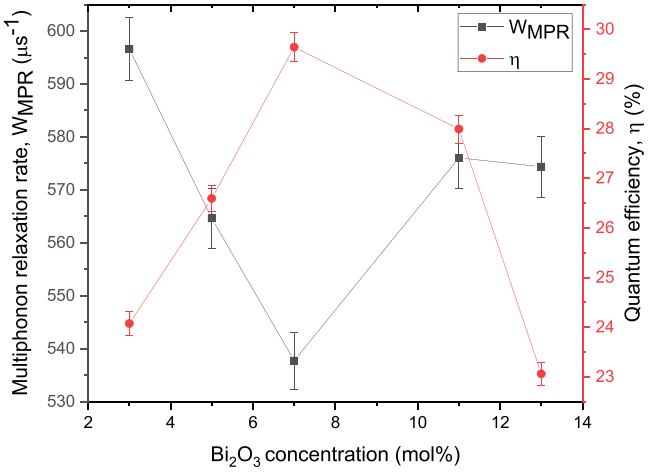

Fig. 8. Multiphonon relaxation rate W_{MPR} and quantum efficiency η of $^4I_{13/2} \rightarrow {}^4I_{15/2}$ transition, under excitation wavelength λ=980 nm of $20Li_2O$-xBi_2O_3-$(78\text{-}x)TeO_2$-$1Er_2O_3$-1Ag glass system increasing Bi_2O_3 concentration.

Table 2
Measured lifetime τ_{mes}, multiphonon relaxation rate W_{MPR}, quantum efficiency η, energy gap ΔE, maximum phonon energy $\hbar w_p$, phonon number P of $^4I_{13/2} \rightarrow {}^4I_{15/2}$ transition, under excitation wavelength λ=980 nm of $20Li_2O$-xBi_2O_3-$(78-x)TeO_2$-$1Er_2O_3$-1Ag glass system.

Bi_2O_3 concentrations (mol%)	Measured lifetime τ_{mes} (μs) ± 30.634	Multiphonon relaxation rate W_{MPR} (μs^{-1}) ± 19.134	Quantum efficiency η (%)± 2.431	Energy gap (cm^{-1}) ΔE ± 1.851	Maximum Phonon Energy $\hbar w_p$ (cm^{-1}) ± 0.84	Phonon number P ± 0.009
3	1275.932	596.581	24.074	6508.368	825.31	7.886
5	1303.068	564.630	26.593	6504.452	827.03	7.865
7	1304.205	537.761	29.641	6503.535	825.31	7.880
11	1248.445	576.066	27.992	6507.325	825.31	7.885
13	1339.875	574.378	23.062	6507.202	827.03	7.868

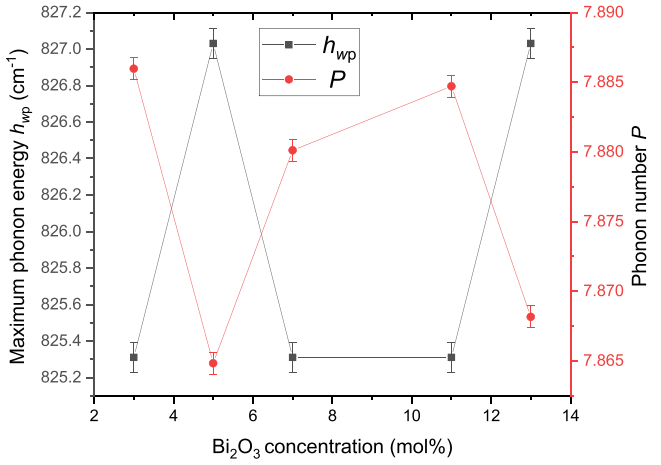

Fig. 9. Maximum phonon energy $\hbar w_p$ of $20Li_2O$-xBi_2O_3-$(78-x)TeO_2$-$1Er_2O_3$-1Ag glass system.and phonon number P bridging $^4I_{13/2} \rightarrow {}^4I_{15/2}$ transition of the glass samples under excitation wavelength λ=980 nm increasing Bi_2O_3 concentration.

3.4. Photoluminescence and energy level analysis

Fig. 10 shows the NIR down-shifting emission spectra. The spectra were within the broad band range from 1450 nm to 1650 nm, which could be attributed to the Er^{3+} transition from the excited state $^4I_{13/2}$ to the ground state $^4I_{15/2}$. The intensity of the $^4I_{13/2} \rightarrow {}^4I_{15/2}$ transition showed an initial increase before a large drop at x=11 mol%, as shown in the inset in Fig. 10. To comprehend the Stark level in the band profile

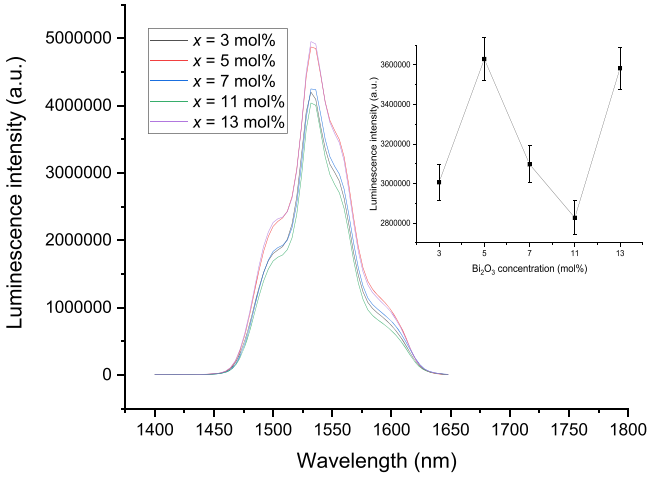

Fig. 10. NIR down conversion emission spectra of $^4I_{13/2} \rightarrow {}^4I_{15/2}$ transition, under excitation wavelength λ=980 nm for $20Li_2O$-xBi_2O_3-$(78-x)TeO_2$-$1Er_2O_3$-1Ag glass system with different amounts of Bi_2O_3 concentration. The inset displays the integrated emission intensities with increasing Bi_2O_3 concentration.

of the $^4I_{13/2} \rightarrow {}^4I_{15/2}$ emission transition of the $20Li_2O$-xBi_2O_3-$(78-x)TeO_2$-$1Er_2O_3$-1Ag glass system, the Gaussian deconvolution for the $^4I_{13/2} \rightarrow {}^4I_{15/2}$ emission transition showed three deconvoluted peaks (Fig. 11). For the various emitting levels, the deconvoluted peak positions indicated all potential transitions between these subcomponents and an equivalent model for the three Stark level systems as shown in the inset in Fig. 11. From the Er^{3+} Stark level diagram (Fig. 11), the excited level $^4I_{13/2}$ populated the three sublevels of ground state $^4I_{15/2}$ (0, 174, 253 cm^{-1}) that contributed to the inhomogeneous broadening of $^4I_{13/2} \rightarrow {}^4I_{15/2}$ emission transition peak in Fig. 10. Hence, the broadening of the peak may lead to overlap between the absorption and fluorescence spectra due to a significant overlap of light waves generated by ions from different Er^{3+} ion sites. The effect of this overlap to the quenching of radiative $^4I_{13/2} \rightarrow {}^4I_{15/2}$ emission will be further discussed in the energy transfer section [53].

Fig. 12 shows the values of the FWHM, which is an important characteristic for laser activity, for the prepared glasses. The broad emission bands with high FWHM values were favorable for a tunable laser medium and could be utilized as a solution for small and efficient eye-safe NIR lasers. The FWHM increased at x<7 mol% before it dropped at x=11 mol%. Furthermore, to determine the rate of energy ejected from the lasing material, the stimulated ECS σ_P^E can be calculated as follows:

$$\sigma_P^E = \frac{\lambda_p^4 A}{8\pi c n^2 \Delta\lambda_{eff}}, \tag{10}$$

where λ_P is the peak wavelength for the emission transition band of the material. In this work, the glass sample with x=11 mol% (Fig. 12) exhibited the maximum cross section stimulated emission σ_P^E than the other glasses. A large ECS value may indicate an effective laser transition, which is suitable for photonic applications, such as solid-state lasers [45].

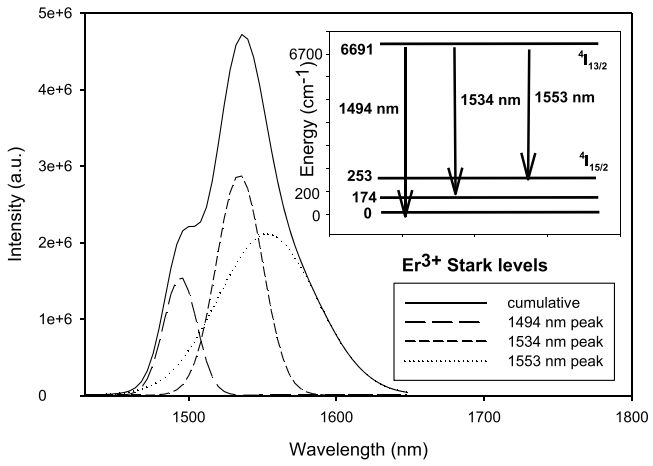

Fig. 11. Gaussian deconvolution of NIR emission spectra of $^4I_{13/2} \rightarrow {}^4I_{15/2}$ transition, under excitation wavelength λ=980 nm for $20Li_2O$-$3Bi_2O_3$-$75TeO_2$-$1Er_2O_3$-1Ag glass system. Inset shows the Stark splitting of $^4I_{13/2} \rightarrow {}^4I_{15/2}$ transition and their energy level diagram.

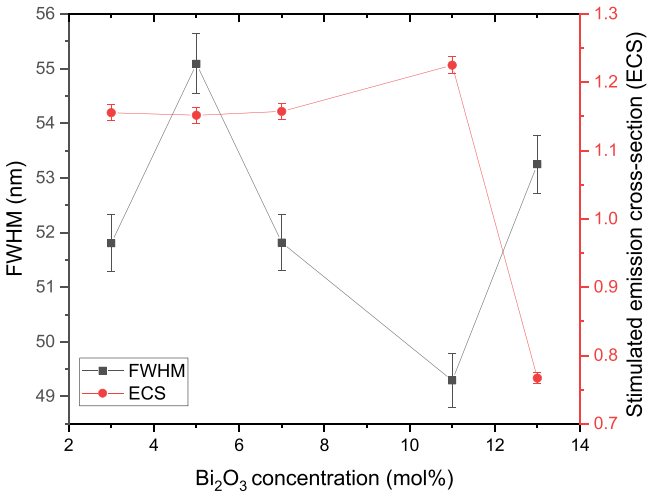

Fig. 12. FWHM and stimulated emission cross-section (ECS) σ_P^E of $^4I_{13/2}\rightarrow{}^4I_{15/2}$ transition, under excitation wavelength λ=980 nm for $20Li_2O$-xBi_2O_3-(78-x) TeO_2-$1Er_2O_3$-1Ag glass system increasing Bi_2O_3 concentration.

3.5. Energy transfer between Er^{3+} ions

As shown in Fig. 6, the energy transfer mechanism occurred from donors (excited ions) to acceptors (unexcited ions) by cross-relaxation at increasing concentrations, resulting in nonexponential behavior of PL decay curves of $^4I_{13/2}\rightarrow{}^4I_{15/2}$ transition [54]. In general, at lower concentrations of acceptor ions, only a small fraction of the total number of excited donor ions is expected to be within the critical distance of the acceptor ions. Meanwhile, a larger fraction of the donor ions is expected to be within the critical interaction range of the acceptors ions as the concentration of the acceptor ions increases [55]. Hence, the interaction between donor and acceptor ions can be represented by the Forster rate of resonance energy transfer k_T as follows [56]:

$$k_T = \left(1/\tau_D^0\right)(R_0/R)^6, \tag{11}$$

where τ_D^0 is the donor fluorescence lifetime in the absence of acceptor, R is the actual donor–acceptor distance, and R_0 is critical transfer distance (Forster distance) in angstrom. The Forster distance is a distance when the rate of transfer is equal to the fluorescence decay rate that may be calculated as follows:

$$R_0^6 = 8.785 \times 10^{-5}\,\kappa^2 Q_D^0 J/n^4, \tag{12}$$

where κ^2 is the interaction between the donor and acceptor molecules, Q_D^0 is the quantum yield, and n is the refractive index of the glass samples. Meanwhile, J is the absorbance acceptor and fluorescence donor emission spectra ($M^{-1}cm^{-1}$), where λ is in nanometer that can be analyzed by the following equation and depicted in the inset in Fig. 15:

$$J = \int F_D(\lambda)\varepsilon_A(\lambda)\lambda^4 d\lambda, \tag{13}$$

where F_D is the peak normalized fluorescence spectrum, and ε_A is the absorption spectrum of the acceptor (Fig. 13). Then, R_0 was used to calculate the donor–acceptor interaction parameter as follows [52]:

$$C_{DA} = R_0\tau_0^{-1}, \tag{14}$$

where τ_0^{-1} is the intrinsic decay rate of the donors, in which τ_0 is the intrinsic fluorescence lifetime. In addition, the energy transfer between the donor and acceptor ions may be analyzed using the Inokuti-Hirayama model as follows [51]:

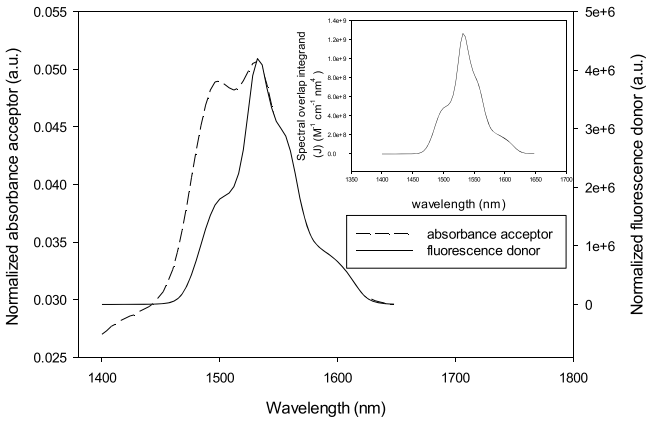

Fig. 13. Absorbance acceptor and fluorescence donor emission spectra of under excitation wavelength λ=980 nm for $20Li_2O$-$3Bi_2O_3$-$75TeO_2$-$1Er_2O_3$-1Ag glass system. Inset shows the overlap integral between the fluorescence spectrum of the donor and the molar absorption spectrum of the acceptor of $^4I_{13/2}\rightarrow{}^4I_{15/2}$ transition.

$$I(t) = I_0 exp\left(-\frac{t}{\tau_0} - \gamma_s\left(\frac{t}{\tau_0}\right)^{3/s}\right), \tag{15}$$

where I_0 denotes the decay intensity at time t=0, τ_0 denotes the intrinsic lifetime, and γ_s denotes the direct energy transfer from the donors to the acceptors. For the electric dipole–dipole, electric dipole–quadrupole, and electric quadrupole–quadrupole interactions, S can take values of 6, 8, and 10. Previous research on Er^{3+} glass has shown that S=6 provides the best match that fit the decay curve rates, indicating that the energy transfer between Er^{3+} ions may be dominated by an electric dipole–dipole interaction. Such phenomenon was carried out via cross relaxations between the $^4I_{13/2}$ and $^4I_{15/2}$ energy levels. Furthermore, γ_s parameter could be calculated as follows by considering the S=6 interaction:

$$\gamma_6 = \frac{4\pi}{3}\,1.77 N_A R_0^3, \tag{16}$$

where N_A is the number density of Er^{3+} ions. In our work, C_{DA} and γ_6 generally increased with a large maximum at x=11 mol% before they dropped at x>11 mol% (Fig. 14). Meanwhile, to verify whether the energy transfer was mainly due to the donor–acceptor clusters or two randomly distributed ions, the shortest distance between two ions D_{random} was calculated as follows [57]:

$$D_{random} = 2\left(\frac{3}{4\pi N_A}\right)^{\frac{1}{3}}, \tag{17}$$

where N_A is the number density of Er^{3+} ions. From Table 3, the D_{random} range values were found to be higher than the R_0 range values. Hence, the energy transfer at $^4I_{13/2}\rightarrow{}^4I_{15/2}$ Er^{3+} transition could be inferred to be mainly due to the Er^{3+} ion donor–Er^{3+} ion acceptor clusters instead of from two randomly distributed ions.

4. Discussion

4.1. AC conductivity and dielectric properties

The variations in σ_{AC} (Fig. 1) can be explained in terms of glass network modification, which occurred when Bi_2O_3 was added to the predominantly ionic tellurite glasses. Given the role of Bi_2O_3 as a glass modifier, at x< 11 mol%, the presence of a substantial fraction of larger Bi^{3+} ions outside the glass network impeded the migration of smaller Li^+ ions as the major charge carriers for ionic conductivity of the glass sample. Hence, further addition of Bi_2O_3 induced a large drop in σ_{AC} at

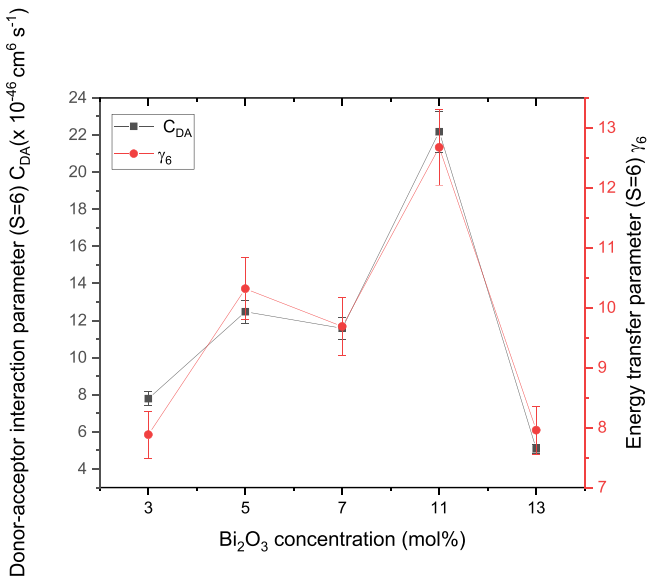

Fig. 14. Donor-acceptor interaction parameter (S=6) C_{DA} and energy transfer parameter (S=6) γ_6 of $^4I_{13/2}\rightarrow{}^4I_{15/2}$ transition under excitation wavelength λ=980 nm for $20Li_2O$-$3Bi_2O_3$-$75TeO_2$-$1Er_2O_3$-1Ag glass system increasing Bi_2O_3 concentration.

Table 3
Critical distance R_0 ($\dot{A}$), donor-acceptor interaction parameter (S=6) C_{DA} (x10^{-46} cm^6 s^{-1}), energy transfer parameter (S=6) γ_6 and shortest distance D_{random} ($\dot{A}$) of $^4I_{13/2}\rightarrow{}^4I_{15/2}$ transition under excitation wavelength λ=980 nm for $20Li_2O$-$3Bi_2O_3$-$75TeO_2$-$1Er_2O_3$-1Ag glass system.

Bi_2O_3 concentrations (mol%)	Critical distance R_0 ($\dot{A}$) ± 0.089	Donor-acceptor interaction parameter (S=6) C_{DA} (x 10^{-46} cm^6 s^{-1}) ± 5.819	Energy transfer parameter (S=6) γ_6 ± 1.765	Shortest distance D_{random} ($\dot{A}$) ± 0.2986
3	1.267	7.793	7.883	15.3977
5	1.352	12.478	10.318	15.0274
7	1.312	11.583	9.688	14.8877
11	1.465	22.176	12.675	15.2024
13	1.198	5.087	7.957	14.5167

x=11 mol%, which could be attributed to the MIE effect. This phenomenon may be related to the blocking effect caused by Bi_2O_3 and, in turn, restricted the mobility of the ionic charge carriers (Fig. 1). In addition, the BiO_6 units accumulated in the interstitial sites of the glass network, impeding the movement of the smaller Li^+ ions. Given its high additional electronic contribution to the total conductivity, the inclusion of Bi_2O_3 was expected to increase the σ_{AC}. However, the σ_{AC} unexpectedly decreased as Bi_2O_3 was increased up to x=11 mol% [58]. The σ_{AC} increased with further addition of Bi_2O_3 at x>11 mol%. This result may due to the role of Bi_2O_3 as a glass former, which induced the formation of large BiO_6 units. Hence, this process may increase the number of acceptor levels and promote polaron hopping, which enhanced the electronic conductivity. Hence, the blocking effect was suggested to be responsible for the alteration in the conduction mechanism from predominantly ionic to predominantly electronic. This inference had been supported by the previous literature, in which the blocking effect was indicated to be responsible for the alteration from predominantly ionic to electronic conductivity in $98[20Li_2O$-xBi_2O_3-$(80$-$x)TeO_2]$-2Ag glass system [59]. Moreover, addition of Bi_2O_3 at x>11 mol% may reduce the polaron hopping distance, enhancing the polaron hopping between transition metal sites and the glass electronic conductivity [59]. Meanwhile, the slight increase in σ_{AC} at x=7 mol% may be due to the formation of NBOs, as shown in the Raman spectra, that promoted the movement of Li^+ ions across the glass network by opening up the glass structure. Two conducting phases may have occurred in the current glass samples, because they were predominantly ionic due to the glass structure Li_2O-TeO_2, until the addition of Bi_2O_3 converted some of the ionic glass structure to Bi_2O_3-TeO_2 electronic glass structure. This phenomenon explain the decreased ionic conductivity and alteration by the emergence of electronic conductivity.

The mechanisms of electronic, ionic, orientational, and space charge polarization generally comprehensively contribute to the dielectric constant of glasses [60]. The nonlinear decrease in the dielectric constant ε for the glass samples at 10^2 Hz frequency (Fig. 2) with the addition of Bi_2O_3 may be due to the presence of the Bi^{3+} ions outside the glass network. Such characteristic impeded the charge carrier movement and formed a short-range pathway for carriers involved in the formation of medium-sized space charge dipoles, resulting in a slower reduction in ε [58]. By contrast, the slight increase in ε at x=7 mol% may be due to the contribution from the formation of NBOs as indicated in the Raman spectra. The formation of NBOs opened the glass network, creating suitable pathways for free Li^+ ions to migrate toward the electrode. This process then contributed to the space charge polarization.

Dielectric loss within the glasses at a specific frequency is described by the loss tangent tan δ. DC conduction losses have been suggested to contribute to tan δ at low frequencies for all glass samples. At low frequencies, charge carriers, such as Li^+ ions, may have hopped repeatedly over a long distance, causing DC conductivity loss. This phenomenon was proven by the 1/ω slope value from the low-frequency dispersion of dielectric loss ε" with increasing frequencies, with values between –0.9516 and –1.3047 (Fig. 3). The slope range showed that the DC conduction loss existed in all glass samples. Interestingly, the decrease in tan δ up to x=11 mol% at 10^2 Hz frequency (Fig. 3) could be attributed to the MIE effect, which reduced the DC conduction losses by impeding the migration of the Li^+ ions in the glass network [59]. Meanwhile, the increase in tan δ at x>11 mol% may be due to the excess free volume formed with further addition of Bi_2O_3 because of the bigger radius of Bi_2O_3 than that of TeO_2. As a result, the glass molar volume increased, thereby facilitating the movement of the charge carrier, resulting an increase in tan δ.

4.2. Decay rates and multiphonon relaxation parameter

The increase in τ_{mes} of up to x=7 mol% (Fig. 7) may be due to the addition of lower phonon Bi_2O_3 that contributed to a decrease in the phonon energy of the glass samples [52]. Meanwhile, a large drop of τ_{mes} at x=11 mol%, which coincided with the large drop in σ_{AC}, may be attributed to the high phonon energy of the glass samples that may associated with the blocking effect. Accumulation of BiO_6 unit at the interstitial sites may have induced thermal vibrations of the glass matrix. This phenomenon led to the increase in vibrational amplitude and optical phonon frequency, contributing to the high phonon energy of the glass samples [61]. In addition, the effect of Er^{3+} ions on the energy transfer process, particularly the high cross-relaxation mechanism γ_6 between the Er^{3+} ions (Fig. 14) as a quenching center, may be the reason for the decrease in the τ_{mes} in the Er^{3+}-doped glasses [62]. Meanwhile, sharp increase in τ_{mes} at x>11 mol% may be attributed to the lowering of the phonon energy of the glass due to further addition of Bi_2O_3. Such augmentation increased the mass of the oxygen ligands, resulting in lower phonon vibration energies [63].

Based on the expression of W_{MPR} in Eq. (4), the MPR rate W_{MPR} was influenced by the phonon density $\rho(\omega)$ and maximum phonon energy $\hbar w_p$. This rate could be analyzed using the Raman spectra (Fig. 4). In general, the decrease in $\rho(\omega)$ and $\hbar w_p$ led to a weaker W_{MPR}. This result suggested that the decrease in the W_{MPR} up to x=7 mol% may have been reasonably caused by the lowering of $\hbar w_p$ (Fig. 9) due to the addition of

lower phonon Bi_2O_3. The reduction in $\hbar w_p$ was due to the decrease in the resonance energy of the lattice vibrations in the glass. which consequently made W_{MPR} less probable. By contrast, W_{MPR} showed a maximum at x=11 mol% which was opposite to the minimum of $\hbar w_p$, indicating that the explanation of W_{MPR} using maximum phonon energy $\hbar w_p$ need to be elucidated [64]. This analysis is consistent with the previous finding by Reisfeld et al., in which the dependency of W_{MPR} to $\hbar w_p$ was just valid for low energy gap (1000 cm^{-1} to 3000 cm^{-1}), low phonon number P (below 5), and high-phonon energy glass, such as B_2O_3. Hence, such $\hbar w_p$ analysis could not be applied to our glass sample due to the high range of energy gap (6503 cm^{-1} to 6508 cm^{-1}), high phonon number (7.87–7.89) and low phonon glass network (TeO_2) [65]. Interestingly, Miyakawa and Dexter [[66]] had proposed phonon-assisted energy transfer probabilities S_{ab} that may occur, which may explain the contrast trend between $\hbar w_p$ and W_{MPR} at x=11 mol% in our glass sample. Phonon-assisted energy transfer S_{ab} may occur if the phonon emission of donor ions is overlapping with the phonon absorption of acceptor ions. Such phenomenon can also be supported by high donor–acceptor interaction parameter C_{DA} and energy transfer parameter γ_6 at x=11 mol% (Fig. 14). The number of phonons is required to be emitted to conserve energy in the MPR process, hence increasing the W_{MPR} but lowering the $\hbar w_p$ of the glass sample [66]. In addition, the high overlap between the phonon emission and absorption between Er^{3+} ions may be explained by the accumulation of BiO_6 in the glass host. Such process may induce vibrational amplitude and optical phonon frequency, contributing to the high phonon-assisted energy transfer S_{ab} at x=11 mol%. The increase in W_{MPR} has also been suggested to be probably related to the increase in σ_{AC} by polaron hopping. Previous research reported the contribution of multiphonon process with electron-lattice coupling to polaronic conductivity. Hence, the MIE effect may have contributed significantly to the multiphonon process, which was favorable for the polaron hopping process during conductivity [67].

In addition, emission cross-section, radiative transition probability, lifetime of the meta stable state, RE ion concentration, and ligand field effects have major influences on the quantum efficiency η of a particular emission transition. Based on the factors that may influence η, the MPR rate W_{MPR} has been suggested to be the main influencing factor due to role of W_{MPR} in enhancing nonradiative transition. Such process decreased the number of photons generated in the radiative transition, which consequently led to the reduction in η as shown by the opposite trend between W_{MPR} and η in Fig. 8 [52].

4.3. Photoluminescence and energy level analysis

The increase in the luminescence intensity of the $^4I_{13/2}\rightarrow{}^4I_{15/2}$ transition (Fig. 10) at x<7 mol% and at x>11 mol% was attributed to the addition of lower phonon Bi_2O_3 that contributed to the lower probability for MPR W_{MPR} to occur. Such phenomenon increased the probability for radiative transition. Meanwhile, the large drop in the luminescence intensity at x=11 mol% may be due to the blocking effect by the BiO_6 units at the interstitial sites. Such blockage may cause thermal vibrations in the glass matrix, increasing the vibrational amplitude and optical phonon frequency and contributing to the high phonon energy of the glass samples. This high phonon energy then increased the probability for MPR W_{MPR} rather than the radiative transition, thereby decreasing the luminescence intensity. In addition, the energy transfer between Er^{3+} ions C_{DA} (Fig. 14) also contributed to a drop in the luminescence intensity at x=11 mol% due to the increased probability for cross relaxation rather than radiative transition. Meanwhile, further addition of Bi_2O_3 at x>11 mol% may have promoted lower phonon energy glass network environment, thereby enhancing the photoluminescence intensity.

The inhomogeneous broadening of the NIR emission band could be due to the increased variation in the environment and coordination number around the Er^{3+} ions. Such phenomenon changed the structure and local crystal field environment of the glasses [52]. Furthermore, the bandwidth (FWHM) was also highly dependent on the overall Stark splitting extent, because the Stark splitting of the ground state was greater than the emission level [68]. The enhanced luminescence FWHM (Fig. 12) at x<7 mol% and x>11 mol% was attributed to the formation of BiO_6 unit, which had high six coordination number by Bi_2O_3 [69,70]. Given the high coordination number of Bi^{3+}, the crystal field of the O^{2-} around the Er^{3+} site expanded, which led to the strong Stark splitting of f-f transitions and induced the broadening of the bandwidth of the 1.55 μm band [70]. Meanwhile, the drop in FWHM at x =11 mol% may due to the role of Bi_2O_3 as glass formers that promoted a high number of BiO_3 units, which have low three coordination number. The low coordination number of Bi^{3+} may have decreased the crystal field of the O^{2-} around the Er^{3+} site, resulting in weak Stark splitting of the f-f transitions and a small broadening of the bandwidth of the 1.55 μm band [70]. Meanwhile, the ECS σ_P^E showed a maximum at x=11 mol%, probably due to addition of high polarizability Bi_2O_3 which contributed for stronger oscillator strength of electric dipole and higher refractive index. Heavy Bi^{3+} ions also promoted the reduction of vibrational frequencies which helped in narrowing electric dipole linewidth thereby leading to high σ_P^E [71].

4.4. Energy transfer between Er^{3+} ions

The increase in C_{DA} and γ_6 values with maximum at x =11 mol% as Bi_2O_3 increased (Fig. 14) may due to the nonradiative cross relaxation, which led to the donor–acceptor energy transfer via dipole–dipole interaction between Er^{3+} ions. This phenomenon caused the non-exponential behavior of the decay rates τ_{mes} and quenching of luminescence. In addition, the high C_{DA} and γ_6 values at x =11 mol% may also indicated the nonradiative behavior of energy transfer as suggested by Malta (2008) in the following energy transfer rate equation W_{ET}, which considered the Franck-Condon factors F [72]:

$$W_{ET} = \frac{2\pi}{h}\left|\langle DA^*|H|D^*A\rangle\right|^2 F, \tag{18}$$

where $|D\rangle$ and $|A\rangle$ represent the donor and acceptor states, respectively. F is directly related to the nonradiative transition rate k_{nr} as described by Marcantonatos as follows [73]:

$$k_{nr} = \beta F, \tag{19}$$

where β is the electronic pre-exponential factor. Hence, the energy transfer that occurred at x=11 mol% could be inferred to be nonradiative in nature. In addition, the F factor is also described to be linearly dependent to electron phonon coupling S as follows:

$$F = \exp -(S)S^{v-1}/(v-1)!, \tag{20}$$

where v is related to the phonon number P as v=P-1. As a consequence, the high nonradiative transition rate k_{nr} due to the phonon-assisted S_{ab} and cross relaxation energy transfer γ_6 may have contributed to the high electron phonon coupling S. This phenomenon may have contributed to the polaron formation and facilitated the polaron transport in the glass matrix at x =11 mol% [74–76].

In addition, the high multiphonon process indicated by the increase of W_{MPR} at x =11 mol% induced the energy transfer from the optical phonons to the electron that induced small polaron formation. Hence, the small polaron formation would contribute to the polaronic conductivity by polaron hopping mechanism as discussed by Mott (1969), who stated that the frequency of optical phonon γ is related to polaron energy W_p as follows [77,78]:

$$\gamma = W_p/\hbar\omega_0, \tag{21}$$

where $\hbar\omega_0$ is the energy of the absorbed photon.

5. Conclusion

Mixed ionic–electronic $20Li_2O$-xBi_2O_3-$(78-x)TeO_2$-$1Er_2O_3$-1Ag glasses had been fabricated. AC conductivity (σ_{AC}) showed a nonlinear decrease at $x \leq 11$ mol% before a large increase at $x>11$ mol% σ_{AC} with increasing Bi_2O_3 concentration. A large drop observed in σ_{AC} at $x=11$ mol% may be due to the MIE effect, which was attributed to the accumulation of BiO_6 units in the interstitial sites of the glass network. This phenomenon impeded the movement of smaller Li^+ ions. The MIE effect in σ_{AC} may have promoted changes in the photoluminescence intensity and lifetime τ_{mes} via structural changes as shown by the Raman spectra. The results from the analysis of nonradiative MPR rate W_{MPR} showed an initial decrease until $x=7$ mol%, indicating the role of lower phonon Bi_2O_3 as glass modifier which promoted higher photoluminescence intensity and lifetime τ_{mes}. The accumulation of BiO_6 units in the interstitial sites of glass network at $x=11$ mol% may have been responsible for the drop in the photoluminescence intensity and lifetime τ_{mes} by increasing the vibrational amplitude of glass network. Such increase contributed to the high phonon energy, which led to the high W_{MPR}. The higher probability of nonradiative multiphonon transition W_{MPR} to occur rather than radiative transition at $x=11$ mol% may have promoted the nonradiative energy transfer via Er^{3+}–Er^{3+} ion cross relaxation γ_6 and phonon-assisted energy transfer S_{ab} at $x=11$ mol%. The nonradiative energy transfer at the MIE region may favor the polaron formation and transport by electron–phonon coupling.

CRediT authorship contribution statement

M.S. Sutrisno: Conceptualization, Data curation, Formal analysis, Investigation, Methodology, Project administration, Resources, Validation, Visualization, Writing – original draft, Writing – review & editing. **H. Nurhafizah:** Validation, Writing – review & editing. **N.S. Sabri:** Funding acquisition, Writing – review & editing. **R. Hisam:** Conceptualization, Formal analysis, Funding acquisition, Investigation, Methodology, Project administration, Resources, Supervision, Validation, Visualization, Writing – review & editing.

Declaration of Competing Interest

The authors declare that they have no known competing financial interests or personal relationships that could have appeared to influence the work reported in this paper.

Acknowledgment

The authors express gratitude to the Research Management Centre (RMC), Universiti Teknologi MARA, Malaysia for assistance throughout the research. This study was financially supported by the Ministry of Higher Education Malaysia under the Fundamental Research Grant Scheme (FRGS), 600-IRMI/FRGS 5/3 (122/2019).

All persons who have made substantial contributions to the work reported in the manuscript (e.g., technical help, writing and editing assistance, general support), but who do not meet the criteria for authorship, are named in the Acknowledgements and have given us their written permission to be named. If we have not included an Acknowledgements, then that indicates that we have not received substantial contributions from non-authors.

References

[1] D. Souri, Fragility, DSC and elastic moduli studies on tellurite–vanadate glasses containing molybdenum, Measurement 44 (10) (2011) 1904–1908.
[2] M.A. Sidkey, A. Abd El-Moneim, L. Abd El-Latif, Ultrasonic studies on ternary TeO_2–V_2O_5–Sm_2O_3 glasses, Mater. Chem. Phys. 61 (2) (1999) 103–109.
[3] M.A. Sidkey, M.S. Gaafar, Ultrasonic studies on network structure of ternary TeO_2–WO_3–K_2O glass system, Physica B 348 (1-4) (2004) 46–55.
[4] M.A. Sidkey, R. El Mallawany, R.I. Nakhla, A. Abd El-Moneim, Ultrasonic studies of (TeO_2) 1-x-(V_2O_5) x glasses, J. NonCryst. Solids 215 (1) (1997) 75–82.
[5] E.C. Cardillo, R.A. Montani, M.A. Frechero, A weak mixed mobile ion effect in vanadium–tellurite oxide glass modified by silver and lithium cations, J. NonCryst. Solids 356 (50-51) (2010) 2760–2763.
[6] Raouf. El-Mallawany, Tellurite glasses part 1. Elastic properties, Mater. Chem. Phys. 53 (2) (1998) 93–120.
[7] T. Sankarappa, M.P. Kumar, G.B. Devidas, N. Nagaraja, R. Ramakrishnareddy, AC conductivity and dielectric studies in V_2O_5–TeO_2 and V_2O_5–CoO–TeO_2 glasses, J. Mol. Struct. 889 (1-3) (2008) 308–315.
[8] G. Lakshminarayana, H. Yang, J. Qiu, Photoluminescence of Pr^{3+}-, and Nd^{3+}-and Ni^{2+}-doped TeO_2–ZnO–WO_3–TiO_2–Na_2O glasses, J. Alloys Compd. 475 (1-2) (2009) 569–576.
[9] N.V. Ovcharenko, T.V. Smirnova, High refractive index and magneto–optical glasses in the systems TeO_2–WO_3–Bi_2O_3 and TeO_2–WO_3–PbO, J. NonCryst. Solids 291 (1-2) (2001) 121–126.
[10] E. Yousef, M. Hotzel, C. Rüssel, Effect of ZnO and Bi_2O_3 addition on linear and nonlinear optical properties of tellurite glasses, J. NonCryst. Solids 353 (4) (2007) 333–338.
[11] F. Chen, B. Song, C. Lin, S. Dai, J. Cheng, J. Heo, Glass formation and third-order optical nonlinear characteristics of bismuthate glasses within Bi_2O_3–GeO_2–TiO_2 pseudo-ternary system, Mater. Chem. Phys. 135 (1) (2012) 73–79.
[12] N. Vijaya, P. Babu, V. Venkatramu, C.K. Jayasankar, S.F. León-Luis, U. R. Rodríguez-Mendoza, V. Lavín, Optical characterization of Er^{3+}-doped zinc fluorophosphate glasses for optical temperature sensors, Sens. Actuators B 186 (2013) 156–164.
[13] C.R. Kesavulu, V.B. Sreedhar, C.K. Jayasankar, K. Jang, D.S. Shin, S.S. Yi, Structural, thermal and spectroscopic properties of highly Er^{3+}-doped novel oxyfluoride glasses for photonic application, Mater. Res. Bull. 51 (2014) 336–344.
[14] Y. Gandhi, N.K. Mohan, N. Veeraiah, Role of nickel ion coordination on spectroscopic and dielectric properties of ZnF_2–As_2O_3–TeO_2: NiO glass system, J. NonCryst. Solids 357 (3) (2011) 1193–1202.
[15] B.C. Jamalaiah, T. Suhasini, L.R. Moorthy, K.J. Reddy, I.G. Kim, D.S. Yoo, K. Jang, Visible and near infrared luminescence properties of Er^{3+}-doped LBTAF glasses for optical amplifiers, Opt. Mater. 34 (5) (2012) 861–867.
[16] D. Ramachari, L.R. Moorthy, C.K. Jayasankar, Gain properties and concentration quenching of Er^{3+}-doped niobium oxyfluorosilicate glasses for photonic applications, Opt. Mater. 36 (4) (2014) 823–828.
[17] K. Selvaraju, N. Vijaya, K. Marimuthu, V. Lavin, Composition dependent spectroscopic properties of Er^{3+}-doped boro-tellurite glasses, *Phys. Status Solidi* (a) 210 (3) (2013) 607–615.
[18] W.A. Pisarski, J. Pisarska, R. Lisiecki, Ł. Grobelny, G. Dominiak-Dzik, W. Ryba-Romanowski, Erbium-doped oxide and oxyhalide lead borate glasses for near-infrared broadband optical amplifiers, Chem. Phys. Lett. 472 (4-6) (2009) 217–219.
[19] L.R.P. Kassab, L.C. Courrol, R. Seragioli, N.U. Wetter, S.H. Tatumi, L. Gomes, Er3+ laser transition in PbO–PbF_2–B_2O_3 glasses, J. NonCryst. Solids 348 (2004) 94–97.
[20] U.R. Rodríguez-Mendoza, E.A. Lalla, J.M. Cáceres, F. Rivera-López, S.F. León-Luís, V. Lavín, Optical characterization, 1.5 μm emission and IR-to-visible energy upconversion in Er^{3+}-doped fluorotellurite glasses, J. Lumin. 131 (6) (2011) 1239–1248.
[21] K. Selvaraju, K. Marimuthu, Structural and spectroscopic studies on concentration dependent Er^{3+} doped boro-tellurite glasses, J. Lumin. 132 (5) (2012) 1171–1178.
[22] Z.A.S. Mahraz, M.R. Sahar, S.K. Ghoshal, M.R. Dousti, Concentration dependent luminescence quenching of Er^{3+}-doped zinc boro-tellurite glass, J. Lumin. 144 (2013) 139–145.
[23] J. Zavadil, Z.G. Ivanova, P. Kostka, M. Hamzaoui, M.T. Soltani, Photoluminescence study of Er-doped zinc–sodium–antimonite glasses, J. Alloys Compd. 611 (2014) 111–116.
[24] K. Ouannes, M.T. Soltani, M. Poulain, G. Boulon, G. Alombert-Goget, Y. Guyot, K. Lebbou, Spectroscopic properties of Er^{3+}-doped antimony oxide glass, J. Alloys Compd. 603 (2014) 132–135.
[25] M.S. Sutrisno, R. Hisam, N.M. Samsudin, Anomalous Behavior of Optical Properties in Mixed Ionic-Electronic $20Li_2O$-xBi_2O_3-$(80-x)TeO_2$ Doped Silver Nanoparticles Tellurite Glass System, Int. J. Electroactive Mater. 7 (2019) 53–66.
[26] S. Rani, S. Sanghi, N. Ahlawat, A. Agarwal, Influence of Bi_2O_3 on thermal, structural and dielectric properties of lithium zinc bismuth borate glasses, J. Alloys Compd. 597 (2014) 110–118.
[27] D. Saritha, Y. Markandeya, M. Salagram, M. Vithal, A.K. Singh, G. Bhikshamaiah, Effect of Bi_2O_3 on physical, optical and structural studies of ZnO–Bi_2O_3–B_2O_3 glasses, J. NonCryst. Solids 354 (52-54) (2008) 5573–5579.
[28] G. Gupta, A.D. Sontakke, P. Karmakar, K. Biswas, S. Balaji, R. Saha, K. Annapurna, Influence of bismuth on structural, elastic and spectroscopic properties of Nd^{3+} doped Zinc–Boro-Bismuthate glasses, J. Lumin. 149 (2014) 163–169.
[29] I. Pal, A. Agarwal, S. Sanghi, M.P. Aggarwal, Structure and optical absorption of Sm^{3+} and Nd^{3+} ions in cadmium bismuth borate glasses with large radiative transition probabilities, Opt. Mater. 34 (7) (2012) 1171–1180.
[30] A. Agarwal, I. Pal, S. Sanghi, M.P. Aggarwal, Judd – Ofelt parameters and radiative properties of Sm^{3+} ions doped zinc bismuth borate glasses, Opt. Mater. 32 (2) (2009).
[31] X. Wang, Q. Nie, T. Xu, X. Shen, L. Liu, The Optic Spectroscopic Analysis & Application in Rare earth doped Bismuth-Tellurite Glasses, in: 2006 IEEE Conference on Robotics, Automation and Mechatronics, IEEE, 2006, pp. 1–5.
[32] B. Zhou, E.Y.B. Pun, H. Lin, D. Yang, L. Huang, Judd–Ofelt analysis, frequency upconversion, and infrared photoluminescence of Ho^{3+}-doped and Ho^{3+}/Yb^{3+}-

codoped lead bismuth gallate oxide glasses, J. Appl. Phys. 106 (10) (2009), 103105.
[33] M. Wang, J. CHeng, M. Li, F. He, Raman spectra of soda–lime–silicate glass doped with rare earth, Physica B 406 (20) (2011) 3865–3869.
[34] I.Z. Hager, R. El-Mallawany, Preparation and structural studies in the (70− x) TeO_2–$20WO_3$–$10Li_2O$–xLn_2O_3 glasses, J. Mater. Sci. 45 (4) (2010) 897–905.
[35] D.R. Neuville, D. de Ligny, G.S. Henderson, Advances in Raman spectroscopy applied to earth and material sciences, Rev. Mineral. Geochem. 78 (1) (2014) 509–541.
[36] S. Damodaraiah, V.R. Prasad, S. Babu, Y.C. Ratnakaram, Structural and luminescence properties of Dy^{3+} doped bismuth phosphate glasses for greenish yellow light applications, Opt. Mater. 67 (2017) 14–24.
[37] J. Jackson, C. Smith, J. Massera, C. Rivero-Baleine, C. Bungay, L. Petit, K. Richardson, Estimation of peak Raman gain coefficients for Barium-Bismuth-Tellurite glasses from spontaneous Raman cross-section experiments, Opt. Express 17 (11) (2009) 9071–9079.
[38] J. He, H. Zhan, A. Lin, Structural property of bismuth-doped tellurite glasses for nonlinear and Raman fiber applications, Opt. Mater. 96 (2019), 109280.
[39] C. Chemarin, B. Champagnon, Medium range order in sodium silicate glasses: role of the network modifier, J. NonCryst. Solids 243 (2-3) (1999) 281–284.
[40] S. Caponi, S. Corezzi, D. Fioretto, A. Fontana, G. Monaco, F. Rossi, Raman-scattering measurements of the vibrational density of states of a reactive mixture during polymerization: effect on the boson peak, Phys. Rev. Lett. 102 (2) (2009), 027402.
[41] F. Qi, F. Huang, L. Zhou, Y. Tian, R. Lei, G. Ren, S. Xu, Long lifetime of Er^{3+}: $^4I_{11/2}$ in low phonon-energy fluoro-chloride glasses for mid-infrared optical applications, J. Alloys Compd. 731 (2018) 418–422.
[42] Y. Ma, X. Wang, L. Zhang, F. Huang, L. Hu, Increased radiative lifetime of Tm^{3+}: $^3F_4 \rightarrow {}^3H_6$ transition in oxyfluoride tellurite glasses, Mater. Res. Bull. 64 (2015) 262–266.
[43] W. Zhang, J. Lin, Y. Jia, S. Zhang, J. Zhao, G. Sun, L. Rong, Enhanced 2–5 μm emission in Ho^{3+}/Yb^{3+} codoped halide modified transparent tellurite glasses, Spectrochim. Acta Part A 134 (2015) 388–398.
[44] S.A. Brawer, W.B. White, Raman spectroscopic investigation of the structure of silicate glasses. I. The binary alkali silicates, J. Chem. Phys. 63 (6) (1975) 2421–2432.
[45] Z.A.S. Mahraz, M.R. Sahar, S.K. Ghoshal, Reduction of non-radiative decay rates in boro-tellurite glass via silver nanoparticles assisted surface plasmon impingement: Judd Ofelt analysis, J. Lumin. 190 (2017) 335–343.
[46] A. Langar, C. Bouzidi, H. Elhouichet, M. Férid, Er–Yb codoped phosphate glasses with improved gain characteristics for an efficient 1.55 μm broadband optical amplifiers, J. Lumin. 148 (2014) 249–255.
[47] L.A. Riseberg, H.W. Moos, Multiphonon orbit-lattice relaxation of excited states of rare-earth ions in crystals, Phys. Rev. 174 (2) (1968) 429.
[48] H. Gebavi, D. Milanese, G. Liao, Q. Chen, M. Ferraris, M. Ivanda, S. Taccheo, Spectroscopic investigation and optical characterization of novel highly thulium doped tellurite glasses, J. NonCryst. Solids 355 (9) (2009) 548–555.
[49] K.A. Gschneidner, J.C.G. Bunzli, V.K. Pecharsky, Handbook on the physics and chemistry of rare earths: optical spectroscopy, Elsevier, 2011.
[50] Q. Chen, M. Ferraris, D. Milanese, Y. Menke, E. Monchiero, G. Perrone, Novel Er-doped PbO and B_2O_3 based glasses: investigation of quantum efficiency and non-radiative transition probability for 1.5 μm broadband emission fluorescence, J. NonCryst. Solids 324 (1-2) (2003) 12–20.
[51] E. Cervantes-Juárez, A.N. Meza-Rocha, W. Romero-Romo, U. Caldiño, C. Falcony, E. Álvarez, R. Lozada-Morales, Up and down-shifting emission properties of novel Er^{3+}-doped CdO-V_2O_5-P_2O_5 glass system, Ceram. Int. 45 (2) (2019) 1609–1615.
[52] S. Arunkumar, K. Marimuthu, Spectroscopic properties of Er^{3+} doped bismuth leadtelluroborate glasses for 1.53 μm optical amplifiers, J. Alloys Compd. 627 (2015) 54–68.
[53] X. Wang, Z. Zhao, Q. Wu, C. Wang, Q. Wang, L. Yanyan, Y. Wang, Structure, photoluminescence and abnormal thermal quenching behavior of Eu^{2+}-doped $Na_3Sc_2(PO_4)_3$: a novel blue-emitting phosphor for n-UV LEDs, J. Mater. Chem. C 4 (37) (2016) 8795–8801.
[54] S. Zhao, X. Wang, D. Fang, S. Xu, L. Hu, Spectroscopic properties and thermal stability of Er^{3+}-doped tungsten–tellurite glass for waveguide amplifier application, J. Alloys Compd. 424 (1-2) (2006) 243–246.
[55] M. Inokuti, F. Hirayama, Influence of energy transfer by the exchange mechanism on donor luminescence, J. Chem. Phys. 43 (6) (1965) 1978–1989.
[56] M.A. Hink, N.V. Visser, J.W. Borst, A. van Hoek, A.J. Visser, Practical use of corrected fluorescence excitation and emission spectra of fluorescent proteins in Förster resonance energy transfer (FRET) studies, J. Fluoresc. 13 (2) (2003) 185–188.
[57] G.U. Caldino, Energy transfer in CaF_2 doped with Ce^{3+}, Eu^{2+} and Mn^{2+} ions, J. Phys. 15 (41) (2003) 7127–7138.
[58] S.N. Mohamed, M.K. Halimah, R.H.Y. Subban, A.K. Yahya, AC conductivity and dielectric properties in mixed ionic–electronic $20Na_2O$–20CaO–(60–x) B_2O_3–xV_2O_5 glasses, Physica B 602 (2021), 412480.
[59] M.S. Sutrisno, N.M. Samsudin, E.S. Sazali, R. Hisam, AC conductivity and dielectric properties of 98 [$20Li_2O$-xBi_2O_3-(80-x)TeO_2]-2Ag mixed ionic-electronic glasses, J. Mater. Sci. Mater. Electron. 32 (4) (2021) 5138–5155.
[60] R. Hisam, A.K. Yahya, H.M. Kamari, Z.A. Talib, AC conductivity and dielectric behavior in mixed electronic-ionic $30Li_2O$–$4MoO_3$–(66–x)TeO_2–xV_2O_5 glass system, Ionics 23 (6) (2017) 1423–1437.
[61] A.A. El-Daly, M.A. Abdo, H.A. Bakr, M.S. Sadeq, Impact of cobalt ions on the phonon energy and ligand field parameters of some borate glasses, J. NonCryst. Solids 555 (2021), 120535.
[62] J.F. Gomes, A.M.O. Lima, M. Sandrini, A.N. Medina, A. Steimacher, F. Pedrochi, M. J. Barboza, Optical and spectroscopic study of erbium doped calcium borotellurite glasses, Opt. Mater. 66 (2017) 211–219.
[63] X. Li, Q. Nie, S. Dai, T. Xu, L. Lu, X. Zhang, Energy transfer and frequency upconversion in Ho^{3+}/Yb^{3+} co-doped bismuth-germanate glasses, J. Alloys Compd. 454 (1-2) (2008) 510–514.
[64] W.S. Tsang, W.M. Yu, C.L. Mak, W.L. Tsui, K.H. Wong, H.K. Hui, Evidence of the influence of phonon density on Tm^{3+} upconversion luminescence in tellurite and germanate glasses, J. Appl. Phys. 91 (4) (2002) 1871–1874.
[65] R. Reisfeld, L. Boehm, Y. Eckstein, N. Lieblich, Multiphonon relaxation of rare earth ions in borate, phosphate, germanate and tellurite glasses, J. Lumin. 10 (3) (1975) 193–204.
[66] T. Miyakawa, D.L. Dexter, Phonon sidebands, multiphonon relaxation of excited states, and phonon-assisted energy transfer between ions in solids, Phys. Rev. B 1 (7) (1970) 2961.
[67] K. Shimakawa, On the mechanism of dc and ac transport in transition metal oxide glasses, Philos. Mag. B 60 (3) (1989) 377–389.
[68] F. Qi, F. Huang, T. Wang, R. Ye, R. Lei, Y. Tian, S. Xu, Highly Er^{3+} doped fluorotellurite glass for 1.5 μm broadband amplification and 2.7 μm microchip laser applications, J. Lumin. 202 (2018) 132–135.
[69] S. Xu, Z. Yang, S. Dai, G. Wang, L. Hu, Z. Jiang, Effect of Bi2O3 on spectroscopic properties of Er^{3+} doped lead oxyfluorosilicate glasses for broadband optical amplifiers, J. NonCryst. Solids 347 (1-3) (2004) 197–203.
[70] Y. Wang, J. Cao, X. Li, J. Li, L. Tan, S. Xu, M. Peng, Mechanism for broadening and enhancing Nd^{3+} emission in zinc aluminophosphate laser glass by addition of Bi_2O_3, J. Am. Ceram. Soc. 102 (4) (2019) 1694–1702.
[71] M.J. Weber, D.C. Ziegler, C.A. Angell, Tailoring stimulated emission cross sections of Nd^{3+} laser glass: observation of large cross sections for $BiCl_3$ glasses, J. Appl. Phys. 53 (6) (1982) 4344–4350.
[72] O.L. Malta, Mechanisms of non-radiative energy transfer involving lanthanide ions revisited, J. NonCryst. Solids 354 (42-44) (2008) 4770–4776.
[73] M.D. Marcantonatos, Multiphonon non-radiative relaxation rates and Judd–Ofelt parameters of lanthanide ions in various solid hosts, J. Chem. Soc. Faraday Trans. 2 82 (3) (1986) 381–393.
[74] C.A. Perroni, V. Cataudella, G. De Filippis, V.M. Ramaglia, Effects of electron-phonon coupling range on the polaron formation, Phys. Rev. B 71 (5) (2005), 054301.
[75] H. Tamura, M. Tsukada, H. Ishii, N. Kobayashi, K. Hirose, Roles of intramolecular and intermolecular electron-phonon coupling on the formation and transport of large polarons in organic semiconductors, Phys. Rev. B 86 (3) (2012), 035208.
[76] G. Kopidakis, C.M. Soukoulis, E.N. Economou, Localization and electron-phonon interactions in disordered systems, EPL (Europhys. Lett.) 33 (6) (1996) 459.
[77] I.G. Austin, N.F. Mott, Polarons in crystalline and non-crystalline materials, Adv. Phys. 18 (71) (1969) 41–102.
[78] N.F. Mott, Conduction in glasses containing transition metal ions, J. NonCryst. Solids 1 (1) (1968) 1–17.